

Coexistence Calculation Using the Isothermal-Isochoric Integration Method

S. Mostafa Razavi,^{1, a)} Richard A. Messerly,^{2, b)} and J. Richard Elliott^{1, c)}

¹⁾ *Department of Chemical and Biomolecular Engineering, The University of Akron, Akron, Ohio 44325, USA*

²⁾ *Thermodynamics Research Center, National Institute of Standards and Technology, Boulder, Colorado 80305, USA*

(Dated: 14 May 2018)

In this work, an isothermal-isochoric integration (ITIC) method is proposed and tested as a viable method for vapor pressure calculation by molecular simulation. Several tests were carried out to validate the method which resulted in less than 1 % deviation from NIST REFPROP values for reduced temperatures of less than 0.85. While consistency is achieved between the ITIC method, Gibbs Ensemble Monte Carlo (GEMC) method, and Grand Canonical Monte Carlo (GCMC) method when reduced temperatures of 0.6-0.85, the ITIC method is much more effective for vapor pressure calculations at reduced temperatures of 0.45-0.6, where relative deviations from experimental data are often quite large but important for practical applications. It is shown that computational efficiency for the complete temperature range is often served best by applying the ITIC method for the entire temperature range rather than applying Monte Carlo (MC) methods for part of the range. Furthermore, the ITIC method lends itself to application with molecular dynamics (MD) as well as MC, advancing the prospect of simulation results that are quantitatively consistent across software platforms.

Keywords: Vapor Pressure, Vapor Liquid Equilibria, Phase Diagram, Liquid Density

I. INTRODUCTION

Phase coexistence determination is important when characterizing the physical properties of a chemical compound. Both the vapor pressure (P^{sat}) and saturation liquid and vapor density (ρ_{liq} and ρ_{vap}) provide sensitive measures of the quality provided by a particular force field. In principle, the computation of phase coexistence is a simple matter of equating pressures, temperatures, and chemical potentials between the coexisting phases. Nevertheless, accurate computation of phase coexistence by molecular simulation has posed challenges over the years.

The most straightforward method to compute phase transition in molecular simulation is to simply define an NVT system (constant number of molecules, volume, and temperature) of sufficient size and overall density that an explicit interface is encountered. However this method often results in imprecise results. First order phase transitions exhibit a considerable free energy barrier between two phases due to interfacial free energies. For systems with large interfaces, this energy barrier increases. This often results in hysteresis, and phase transformation irreversibly proceeds beyond the coexistence point.¹

Alternatively, there are methods for calculating phase coexistence while avoiding explicit interfaces. The Gibbs Ensemble Monte Carlo (GEMC) method² is one of the most popular phase coexistence determination methods³.

The GEMC method requires particle exchange between two phases which leads to its major drawback, i.e. insertion of particles in dense phases for large molecules. This problem is especially exacerbated at low temperatures. The lowest temperatures that are typically available in the literature rarely extend below a reduced temperature ($T_r = T/T_c$, where T_c is the critical temperature) of 0.6^{4,5}. However, common methods for industrial applications treat the temperature range from $T_r = 0.45$ to critical point. The Peng-Robinson equation of state, for example, is valid for reduced temperatures as low as 0.45.⁶ To provide fundamental physical models that address issues with industrial applications, molecular simulations must address the entire temperature range of interest.

As another alternative, Kofke⁷ developed a method called Gibbs-Duhem integration which makes use of the Clapeyron equation to numerically integrate and proceed along the saturation line starting from one single coexistence point. The Gibbs-Duhem method can solve the insertion problem, but it provides a limited extension beyond the starting coexistence point, and it relies on a second method to obtain the initial coexistence point. Ahunbay et al.⁸ have applied this approach but their implementation has not been tested below a reduced temperature of 0.55.

As one more alternative, thermodynamic integration can provide a reliable solution for free energy calculation. In this method, a series of simulations are performed along a path that connects the state of interest to a system for which the free energy is known. One should be careful that the path does not include any type of phase change. For example, Elliott et al.⁹ applied an isochoric integration method to calculate vapor-liquid equilibria of square well spheres, demonstrating deficiencies in the

^{a)} Electronic mail: sr87@uakron.edu

^{b)} Electronic mail: richard.messerly@nist.gov

^{c)} Electronic mail: elliott1@uakron.edu

preceding MC results. For square well spheres, a convenient starting isotherm was the hard sphere limit, for which the thermodynamics are well represented by the Carnahan-Starling equation¹⁰. In this work, however, results are sought for soft potential models of arbitrary molecular shape, for which the infinite temperature limit is not convenient.

In the proposed method, simulation points are used across an isotherm and along isochores, hence the name isothermal-isochoric (ITIC) was chosen. Because the approach to low temperatures proceeds along an isochore initialized at the high temperature (supercritical) isotherm, insertion is not a problem. In principle, there is no lower limit for the applicability of this method, except the triple point. Also, the data generated along the path of integration are valuable on their own merits, providing distinct insights about how well the molecular model is performing under conditions of high temperature and pressure. In other words, ITIC provides greater quality of characterization than MC methods at both higher temperatures and lower temperatures.

As another advantage, vapor pressure calculation using molecular dynamics is often perceived as an impractical approach¹¹. In this work, we will show the possibility of using molecular dynamics in the context of ITIC integration as a viable tool for vapor pressure calculation without a significant increase in computational effort compared to the typical approach of applying GEMC.

The presentation is initiated in Section II with a brief review of the thermodynamics underlying the integration method, including the manner in which characterizing the virial coefficients leads to simple but accurate coexistence determination. The approach is validated in Section III A by applying it to coexistence data available from the National Institute of Standards and Technology (NIST). Sensitivity of the method to the virial coefficients is explored in Section III B. Section IV provides recommendations for the most convenient and effective methods for characterizing the virial coefficients by molecular simulation. Section V investigates the magnitude of finite size effects. Section VI and Section VII demonstrate applications to molecular simulations and comparison between ITIC method and other methods of phase coexistence calculation.

II. ISOTHERMAL-ISOCHORIC INTEGRATION METHOD

For a single component system, Eq. (1) must be satisfied at vapor-liquid phase equilibrium

$$\begin{aligned} T^{\text{vap}} &= T^{\text{liq}} \\ P^{\text{vap}} &= P^{\text{liq}} \\ G^{\text{vap}} &= G^{\text{liq}} \end{aligned} \quad (1)$$

where G represents Gibbs free energy, and superscripts “vap” and “liq” denote the vapor and liquid phases, respectively. As mentioned in Section I, calculating free

energy of a system using the ITIC integration method involves connecting the state of interest to a state of known free energy. In the case of phase equilibrium calculation, the state of interest is saturated liquid and the state of known free energy is an ideal gas. In order to go from saturated liquid to low densities we cannot directly pass through the two phase region. To overcome this problem we take an alternative path. First, the temperature of saturated liquid is increased to a supercritical temperature (isochore). Second, the supercritical state is rarefied to low densities (isotherm). It is worth mentioning that this method requires several separate simulations in the canonical ensemble (NVT) to provide enough data points on the paths for numerical integration to be accurate. Isochoric and isothermal pathways are shown in Fig. 1. The first stage involves integrating internal energy, U , according to Eq. (6) which is derived using Eqs. (2-5):

$$U = kT^2 \left(\frac{\partial \ln Q}{\partial T} \right)_{N,V} \quad (2)$$

$$A(N, V, T) = -kT \ln Q(N, V, T) \quad (3)$$

$$U = kT^2 \left(\frac{\partial(-A/kT)}{\partial T} \right)_{N,V} = \frac{\partial \beta A}{\partial \beta} \quad (4)$$

$$\beta A = \int U d\beta + \text{constant} \quad (5)$$

$$\frac{A - A^{\text{ig}}}{RT} = \int (U - U^{\text{ig}}) d \left(\frac{1}{RT} \right) \quad (6)$$

where V represents volume, R is the gas constant, k is the Boltzmann constant, A is the Helmholtz energy, Q is the canonical partition function, $\beta \equiv \frac{1}{kT}$, and superscript “ig” denotes the ideal gas. Eq. 6 is obtained from Eq. 5 by taking the difference between the real and ideal gas states (where the constants of integration cancel). Note that $k = \frac{R}{N_A}$, where N_A is Avogadro’s number.

The second stage consists in performing the following integration:

$$\frac{A - A^{\text{ig}}}{RT} = \int_0^\rho \frac{Z - 1}{\rho} d\rho \quad (7)$$

where ρ represents density and Z is the compressibility factor ($Z \equiv \frac{P}{\rho RT}$).

Therefore, the Helmholtz energy departure function of the liquid phase is calculated by integrating $(Z - 1)/\rho$ from zero to the saturated liquid density of interest along the supercritical isotherm ($T^{\text{IT}} \approx 1.2 T_c$), added to the Helmholtz energy calculated by integrating internal energy departure function with respect to $1/T$ along the saturated liquid density isochore from $T_r \approx 1.2$ to saturation temperature

$$\frac{A^{\text{liq}} - A^{\text{ig}}}{RT} = \int_0^{\rho_{\text{liq}}} \frac{Z-1}{\rho} d\rho \Big|_{T^{\text{IT}}} + \int_{T^{\text{IT}}}^{T^{\text{sat}}} (U - U^{\text{ig}}) d\left(\frac{1}{RT}\right) \Big|_{\rho_{\text{liq}}} \quad (8)$$

The Gibbs energy criterion of phase equilibrium shown in Eq. (1) can be rewritten in departure function form as shown in Eq. (9).

$$\frac{G^{\text{liq}} - G^{\text{ig}}}{RT} = \frac{G^{\text{vap}} - G^{\text{ig}}}{RT} \quad (9)$$

which can be rearranged in terms of the Helmholtz energy departure function

$$\begin{aligned} & \left(\frac{A^{\text{liq}} - A^{\text{ig}}}{RT} \right)_{T,V} + Z_{\text{liq}} - 1 - \ln(Z_{\text{liq}}) \\ &= \left(\frac{A^{\text{vap}} - A^{\text{ig}}}{RT} \right)_{T,V} + Z_{\text{vap}} - 1 - \ln(Z_{\text{vap}}) \end{aligned} \quad (10)$$

Note that the $\ln(Z)$ terms in Eq. (10) are introduced when converting Gibbs energy departure function at constant T, P in Eq. (9) to Helmholtz energy departure function at constant T, V in Eq. (10).

The value for Z_{vap} in Eq. (10) can be approximated using a virial expansion truncated at the B_3 term

$$Z_{\text{vap}} = 1 + B_2 \rho_{\text{vap}} + B_3 \rho_{\text{vap}}^2 \quad (11)$$

Therefore,

$$\begin{aligned} & \left(\frac{A^{\text{vap}} - A^{\text{ig}}}{RT} \right)_{T,V} = \int_0^{\rho_{\text{vap}}} \frac{Z-1}{\rho} d\rho \\ &= \int_0^{\rho_{\text{vap}}} \frac{B_2 \rho_{\text{vap}} + B_3 \rho_{\text{vap}}^2}{\rho_{\text{vap}}} d\rho_{\text{vap}} = B_2 \rho_{\text{vap}} + \frac{1}{2} B_3 \rho_{\text{vap}}^2 \end{aligned} \quad (12)$$

Substituting Eq. (11) and Eq. (12) in Eq. (10) yields

$$\begin{aligned} & \left(\frac{A^{\text{liq}} - A^{\text{ig}}}{RT} \right)_{T,V} + Z_{\text{liq}} - 1 - \ln\left(\frac{P}{\rho_{\text{liq}} RT}\right) \\ &= B_2 \rho_{\text{vap}} + \frac{1}{2} B_3 \rho_{\text{vap}}^2 + B_2 \rho_{\text{vap}} + B_3 \rho_{\text{vap}}^2 - \ln\left(\frac{P}{\rho_{\text{vap}} RT}\right) \end{aligned} \quad (13)$$

Rearranging Eq. (13) gives

$$\frac{A^{\text{liq}} - A^{\text{ig}}}{RT} + Z_{\text{liq}} - 1 + \ln\left(\frac{\rho_{\text{liq}}}{\rho_{\text{vap}}}\right) = 2B_2 \rho_{\text{vap}} + \frac{3}{2} B_3 \rho_{\text{vap}}^2 \quad (14)$$

which can be rearranged further to solve for ρ_{vap}

$$\begin{aligned} & \rho_{\text{vap}} = \\ & \rho_{\text{liq}} \exp\left(\left(\frac{A^{\text{liq}} - A^{\text{ig}}}{RT}\right)_{T,V} + Z_{\text{liq}} - 1 - 2B_2 \rho_{\text{vap}} - \frac{3}{2} B_3 \rho_{\text{vap}}^2\right) \end{aligned} \quad (15)$$

Eq. (14) (or Eq. (15)) is solved for vapor density using the fixed-point iteration method¹² starting from an initial (low density) guess. Once vapor density is calculated, Eq. (16) gives the vapor pressure.

$$P_{\text{vap}} = Z_{\text{vap}} \rho_{\text{vap}} RT = (1 + B_2 \rho_{\text{vap}} + B_3 \rho_{\text{vap}}^2) \rho_{\text{vap}} RT \quad (16)$$

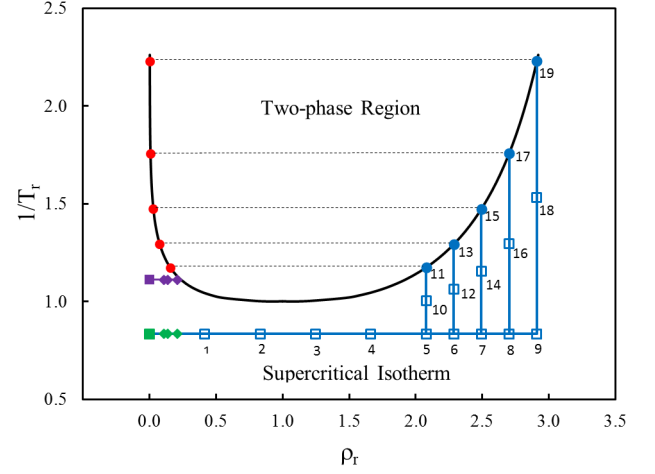


FIG. 1. A schematic plot of the pathways taken in the ITIC method for ethane. The y-axis represents the reciprocal reduced temperature and the x-axis shows the reduced density. All the values were taken from NIST REFPROP¹⁴. Circles represent coexistence points while squares and diamonds represent non-saturated state points. Green and purple points show the state points required for B_2 calculation at isothermal temperature and $T_r = 0.9$, respectively.

In order to obtain any saturation point, one needs to proceed through one isothermal and one isochoric path, to be able to calculate the free energy. The ITIC methodology was tested and validated using NIST Reference Fluid Properties (REFPROP)¹³ values by which the minimal number of data points on each path required to achieve reliable results was determined. In order to reach the densities of interest and maintain an acceptable accuracy to a reduced temperature of 0.45, one needs at least 9 data points on the isotherm and three data points on the isochore for each saturation point. The highest temperature state points, however, serve on both isochores and isotherm, hence these points are only simulated once. Therefore, a total of 19 state points are required to obtain 5 coexistence conditions. Fig. 1 provides a schematic plot of these state points. The isotherm is constructed at a supercritical temperature. A reduced temperature of $T_r \approx 1.2$ was the default value for the isotherm. For some compounds, owing to lack of NIST REFPROP values at high temperatures and the desire to compare isochores and isotherms to NIST REFPROP values when possible, a lower reduced temperature ($T_r \approx 1.05$) was chosen for the isotherm. Validations against NIST REFPROP values showed that any reduced temperature from 1.05 to 1.2 leads to acceptable accuracy.

The integrations along the isotherm and isochores are performed using Simpson's rule¹⁵. Eq. (17) and Eq. (18) are articulations of Simpson's rule used for numerical integration along the isotherm and isochores to calculate A^{dep} by Eq. (8).

$$\int_a^b f(x)dx \approx \frac{b-a}{6} \left[f(a) + 4f\left(\frac{a+b}{2}\right) + f(b) \right] \quad (17)$$

$$\int_a^b f(x)dx \approx \frac{b-a}{8} \left[f(a) + 3f\left(\frac{b-a}{3}\right) + 3f\left(\frac{2(b-a)}{3}\right) + f(b) \right] \quad (18)$$

The A^{dep} values at points 2, 4, 7, and 9 in Fig. 1 are calculated using Eq. (17) in which the value of function at three equidistant points on the x-axis are needed. The A^{dep} values at points 3, 5, and 8 are calculated using Eq. (18) in which the value of the function at four equidistant points on the x axis are needed. The A^{dep} at point 6 is equal to the integration value from point 6 to point 8 subtracted from the A^{dep} value at point 8. The A^{dep} value at point 1 is equal to the integration value from point 1 to point 4 subtracted from A^{dep} value at point 4. The green diamonds in Fig. 1 are used in estimating B_2 at isothermal temperature (green square) which is an essential part of ITIC integration. The purple diamonds are simulated to obtain a B_2 correlation for certain compounds for which B_2 at saturation temperatures were not available. The low density simulations (green diamonds and purple diamonds) are extrapolated to $\rho = 0$ to estimate B_2 . Note that the value of $(Z - 1)/\rho$ at $\rho = 0$ is equal to the second virial coefficient. This method is discussed in detail in Section IV.

III. ITIC VALIDATION

A. Validation using NIST REFPROP

A simple way to test the accuracy of the ITIC method is to use a database that provides precise and self-consistent saturation properties and isochoric/isothermal properties. NIST Reference Fluid Properties (REFPROP) provides such values^{13,14,16,17}, which were used to validate the ITIC method. The following comparisons are solely based on NIST REFPROP equations, therefore the lack of statistical noise inherent to molecular simulation allows performing numerical integration very accurately.

Fig. 2 and Fig. 3 show the ITIC validation results for *n*-dodecane when virial expansion in Eq. (11) includes B_3 term. The deviations of calculated P^{sat} , $\rho_{\text{liq}}^{\text{sat}}$, $\rho_{\text{vap}}^{\text{sat}}$, and ΔH_v from the data obtained directly from NIST REFPROP¹⁶ are provided in Table I. According to this table, one can reach a reduced saturation temperature (T_r^{sat}) of 0.9 with less than 1 % error in vapor pressure. The ITIC method fails to calculate accurate vapor pressure when $T_r^{\text{sat}} > 0.9$. If the B_3 term is excluded from Eq. (11), the ITIC method fails for $T_r^{\text{sat}} > 0.85$. Table II list the deviations from NIST REFPROP saturation data

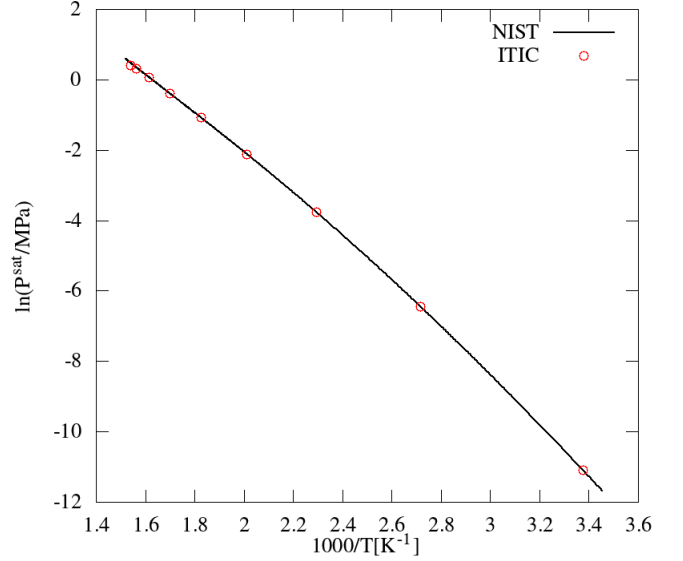


FIG. 2. P^{sat} plot of *n*-dodecane. ITIC results are obtained using NIST REFPROP values¹⁶ for U^{dep} and Z . B_3 is included in Eq. (15).

when B_3 is not used. As shown in this table, the ITIC method provides less than 1 % deviation in vapor pressure when $T_r^{\text{sat}} < 0.85$.

Fig. 4 illustrates the convergence paths taken by a fixed-point method to calculate ρ_{vap} . Fig. 5 shows the same plot, except B_3 is excluded, i.e. virial expansion in Eq. (11) is truncated at B_2 term. Using B_3 corrects the curve representing the right-hand side of Eq. (15) ($g(\rho_{\text{vap}})$) in such a way that fixed-point iteration converges.

The vapor pressure was shown to be sensitive to the value of B_3 at saturation condition. This sensitivity and the sensitivity of vapor pressure to accuracy of B_2 at saturation temperatures as well as supercritical isothermal temperature is characterized in Section IIIB.

B. Vapor Pressure Sensitivity to Virial Coefficients

In order to estimate the required accuracy of the second virial coefficient at the isothermal temperature (i.e. $(Z - 1)/\rho$ at $\rho = 0$), Fig. 6 was generated by changing B_2 and calculating the corresponding deviations in *n*-dodecane vapor pressure. For example, P^{sat} changes by around 5 % if B_2 at isotherm changes by 20 %, and a 5 % change in B_2 results in around 2 % deviation in *n*-dodecane's P^{sat} . The sensitivity is almost independent of saturation reduced temperatures (T_r^{sat}). This shows that it is imperative to use an accurate B_2 value at the isothermal temperature.

Vapor pressure precision is very weakly influenced at low temperatures by accuracy of the second and third virial coefficients in Eq. (15) and Eq. (16). Fig. 7 shows

TABLE I. Accuracy of the ITIC method for *n*-dodecane when third virial coefficient is used

T_r^{sat}	[K] T^{sat}	[MPa] P^{sat}	% Dev. ^a	[g/cm ³] ρ_{liq}	% Dev.	[g/cm ³] ρ_{vap}	% Dev.	[kJ/mol] ΔH_v	% Dev.
0.987	649.33	1.5170088	-6.08	0.3202	-7.19	0.078389	-34.28	15.63	19.06
0.973	640.48	1.3808947	-3.70	0.3736	-0.80	0.072090	-22.69	18.97	11.09
0.942	619.73	1.0598150	-1.53	0.4269	-0.02	0.054262	-8.37	24.15	3.09
0.895	588.88	0.6788865	-0.28	0.4803	0.03	0.032482	-1.57	30.46	1.36
0.833	548.06	0.3423508	-0.07	0.5336	0.01	0.015427	-0.26	36.89	0.95
0.755	496.92	0.1206953	0.03	0.5870	0.01	0.005419	0.01	43.04	0.52
0.663	436.21	0.0234394	-0.08	0.6404	0.00	0.001129	-0.08	48.99	0.19
0.559	368.12	0.0015922	0.09	0.6937	0.00	0.000089	0.10	55.06	0.04
0.450	296.21	0.0000153	0.46	0.7471	0.00	0.000001	0.89	61.76	0.01

^a Deviations are calculated using $\frac{\text{ITIC}-\text{NIST}}{\text{NIST}} \times 100$

TABLE II. Accuracy of the ITIC method for *n*-dodecane when third virial coefficient is not used. For $T_r^{\text{sat}} > 0.9$ the fixed-point iteration does not converge.

T_r^{sat}	[K] T^{sat}	[MPa] P^{sat}	% Dev.	[g/cm ³] ρ_{liq}	% Dev.	[g/cm ³] ρ_{vap}	% Dev.	[kJ/mol] ΔH_v	% Dev.
0.935	615.05	-2.5523492	-353.51	0.3202	-26.60	0.172892	220.25	1.20	-95.14
0.942	619.6	-2.7091311	-352.18	0.3736	-12.56	0.177782	200.99	2.64	-88.74
0.928	610.4	-1.4359029	-252.54	0.4269	-4.04	0.150039	204.09	9.18	-64.22
0.895	589.1	0.7097525	3.89	0.4803	0.10	0.040847	23.28	28.90	-3.70
0.833	548.07	0.3448984	0.65	0.5336	0.02	0.015851	2.46	36.77	0.61
0.755	496.92	0.1208125	0.13	0.5870	0.01	0.005436	0.33	43.03	0.49
0.663	436.21	0.0234409	-0.08	0.6404	0.00	0.001129	-0.06	48.99	0.19
0.559	368.12	0.0015922	0.09	0.6937	0.00	0.000089	0.10	55.06	0.04
0.450	296.21	0.0000153	0.46	0.7471	0.00	0.000001	0.89	61.76	0.01

the P^{sat} sensitivity to B_2 at various reduced temperatures, each representing one isochore. The first three lowest temperatures, are barely sensitive to B_2 precision such that even 50 % error in B_2 results in less than 1 % deviation in P^{sat} . However, a relatively accurate B_2 is required to obtain accurate P^{sat} when $T_r > 0.75$. Similarly, at $T_r = 0.84$ one needs to stay below 2 % deviation in B_2 in order to have less than 1 % error in vapor pressure.

Above a certain reduced temperature (around 0.85), as illustrated in Fig. 8, the ITIC method fails to converge when B_3 is neglected. This leads to the unusual behavior of the $T_r = 0.89$ plot in Fig. 6 and 7. This upper limit can be increased by using the B_3 term in Eq. (15) and Eq. (16) which will help the ρ_{vap} to converge, as can be seen in Fig. 9.

Fig. 10 was plotted similar to Fig. 7, except B_3 term was added. It is worth mentioning that in order to truly understand the influence of B_3 , exact values of B_2 were used from NIST REFPROP. Even though adding B_3 improves the overall behavior of fixed-point iteration in terms of convergence (Fig. 4 and Fig. 5), the sensitivity of P^{sat} to B_3 is negligible when T_r is less than 0.85. This supports the idea of setting the B_3 term to zero without significant loss of precision at such temperatures.

IV. VIRIAL COEFFICIENTS CALCULATION

Second virial coefficients can be estimated by calculating the intercept of $(Z - 1)/\rho$ with respect to ρ . In principle, the slope of this line at zero density gives the third virial coefficient. Fig. 11 shows the accuracy of this method when used at various temperatures. The intercept and slope of the blue lines in this figure represent Schultz's¹⁸ values of B_2 and B_3 , respectively. These lines are plotted using Eq. (19)

$$\frac{Z - 1}{\rho} = B_2 + B_3\rho \quad (19)$$

It is shown for TraPPE-UA ethane that at temperatures above $T_r = 0.80$, B_2 values calculated using this method are consistent with values reported by Schultz. At the two lowest temperatures in Fig. 11 the highest density point is not in line with the blue lines due to being in the two-phase region, therefore using the first three points for those temperatures gives a more accurate estimate of B_2 (green triangle).

According to Eq. (15), it is important to have a correlation for B_2 and B_3 with respect to temperature, because temperatures change after each iteration and updated values for B_2 and B_3 are needed. In order to obtain such a correlation, the formula used in the DIPPR²¹ database

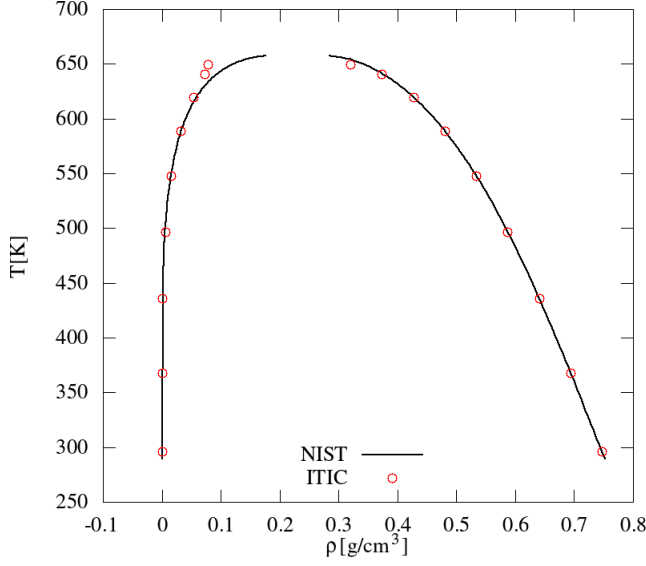


FIG. 3. Coexistence curves of *n*-dodecane. ITIC results are obtained using NIST REFPROP values¹⁶ for U^{dep} and Z . B_3 is included in Eq. (15).

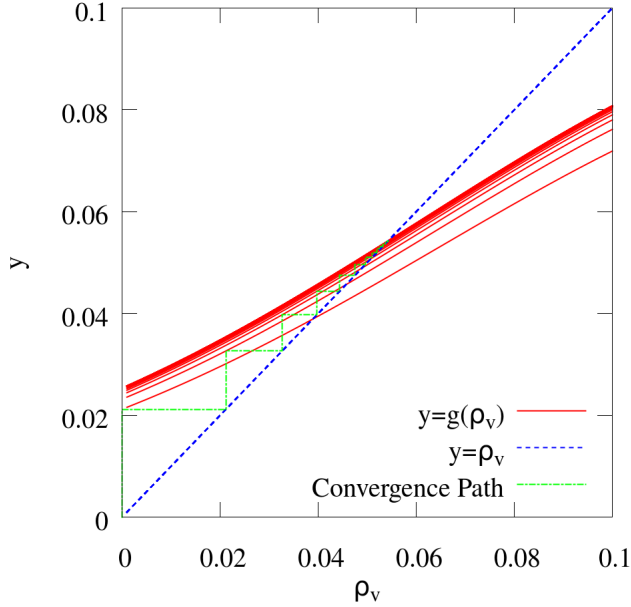


FIG. 4. Fixed-point method iteration and convergence path for *n*-dodecane for the isochore corresponding to $\rho_{\text{liq}} = 0.4269 \text{ g/cm}^3$ when B_3 is used in Eq. (11). Eq. (15) is summarized into $\rho_{\text{vap}} = g(\rho_{\text{vap}})$, i.e. the standard form of fixed-point method. The blue line represents the 45-degree line. The $g(\rho_{\text{vap}})$ curves represent the right-hand side of Eq. (15). At each iteration, $g(\rho_{\text{vap}})$ is calculated based on a new set of T^{sat} , A_L^{dep} , and Z_L . Iteration starts with a low initial guess for ρ_{vap} and stops when absolute percent deviation between two consecutive ρ_{vap} values is less than a small tolerance, e.g. 0.1 %.

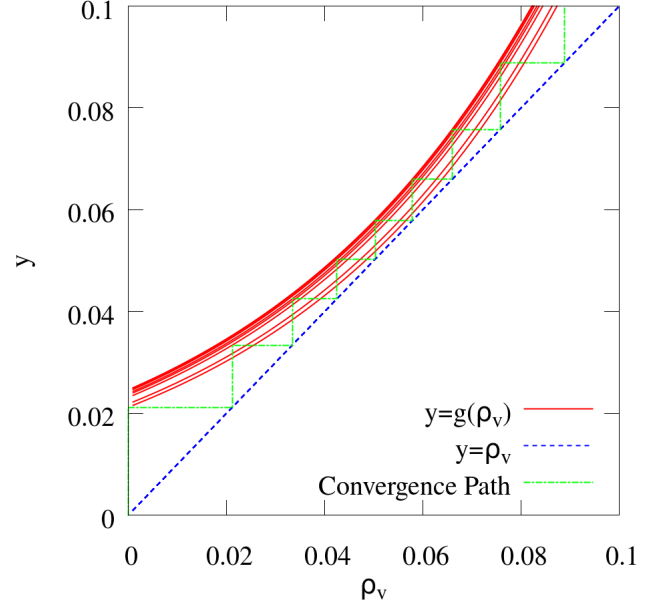


FIG. 5. Fixed-point method iteration and convergence path. The only difference between this figure and Fig. 4 is that B_3 term is excluded from Eq. (11)

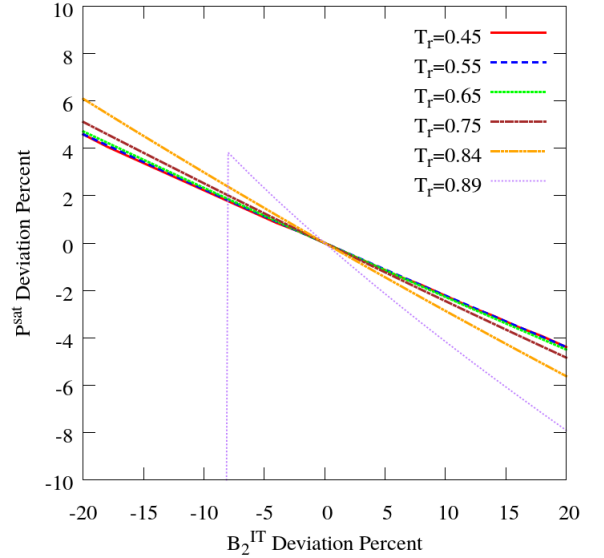


FIG. 6. P^{sat} sensitivity to isotherm B_2

was adapted, except the last term was removed to decrease the number of parameters and avoid overfitting, as shown in Eq. (20)

$$B_2 = A + \frac{B}{T} + \frac{C}{T^3} \quad (20)$$

Taking the derivative of B_2 with respect to β leads

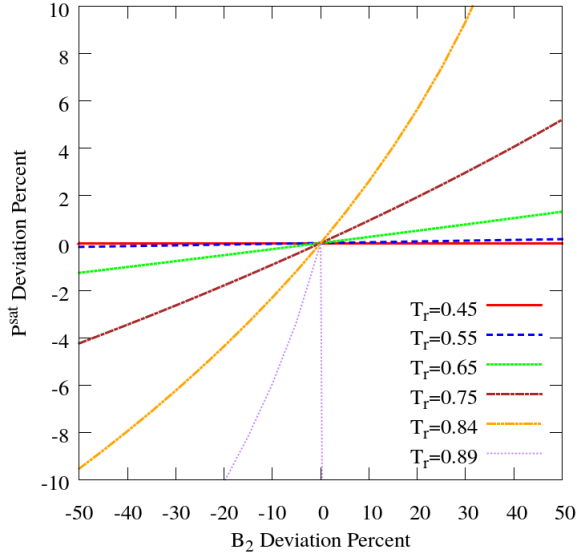


FIG. 7. P^{sat} sensitivity to second virial coefficient used in Eq. (16)

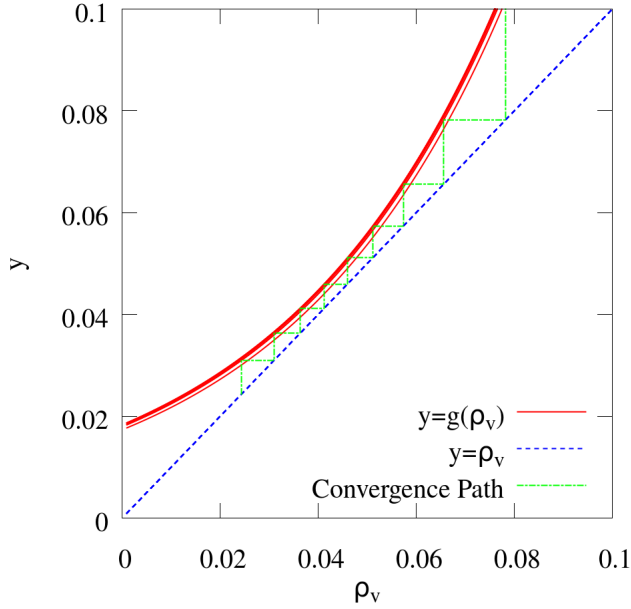


FIG. 8. Fixed-point iteration path at reduced temperature of $T_r = 0.89$. In this case, B_2 is not sufficient and B_3 is required.

to the internal energy departure function, as shown in Eq. (21)

$$\rho \frac{\beta \partial B_2}{\partial \beta} = \rho \left(\frac{B}{T} + \frac{3C}{T^3} \right) = \frac{U - U^{\text{ig}}}{RT} \quad (21)$$

Eq. (22) and Eq. (23) are obtained by inserting B_2 values extrapolated using Eq. (19) and their corresponding

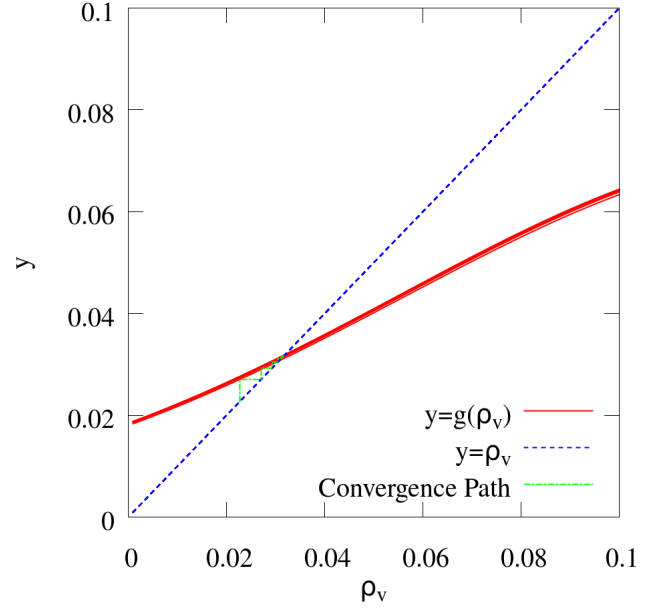


FIG. 9. Convergence path at reduced temperature of $T_r = 0.89$. B_3 term helps the fixed-point iteration to converge.

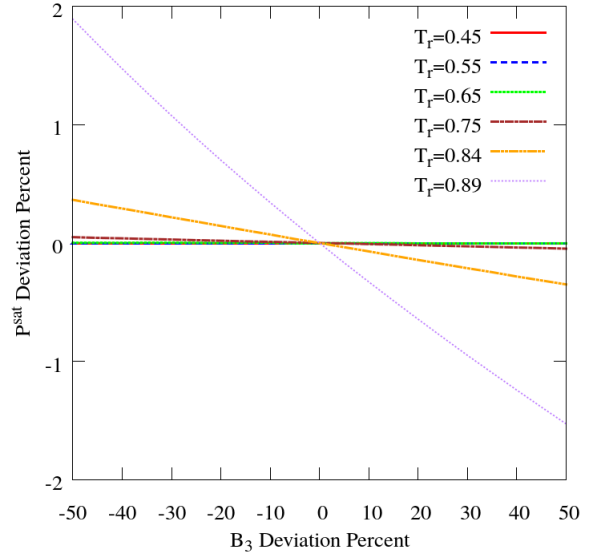


FIG. 10. P^{sat} sensitivity to third virial coefficient used in Eq. (16)

temperatures into Eq. (20).

$$B_2(T_{\text{IT}}) = A + \frac{B}{T_{\text{IT}}} + \frac{C}{T_{\text{IT}}^3} \quad (22)$$

$$B_2(T_{0.9}) = A + \frac{B}{T_{0.9}} + \frac{C}{T_{0.9}^3} \quad (23)$$

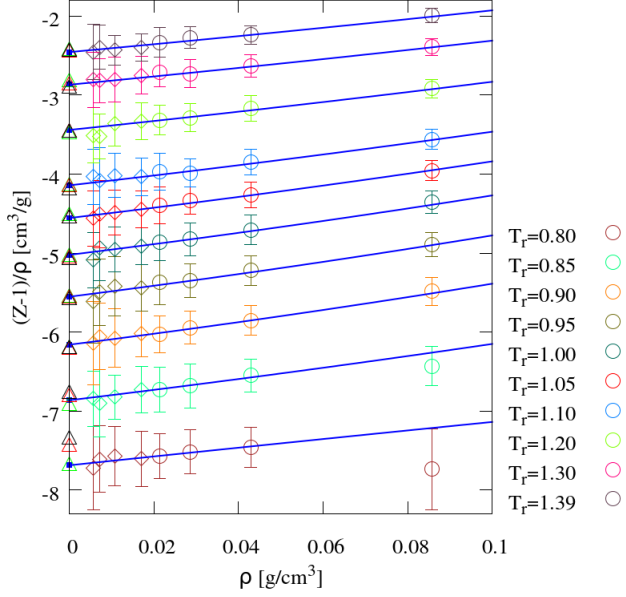


FIG. 11. Plot of $(Z - 1)/\rho$ with respect to ρ for ethane. Blue solid points represent Schultz's B_2 values in Ref. 8. Each blue line represents Schultz values of intercept (B_2) and slope (B_3) at corresponding temperatures. Circles and diamonds are NVT state points simulated in GOMC (GPU Optimized Monte Carlo) package¹⁹. Diamond points are very low density simulations that were not used in B_2 and B_3 calculations. Black, green, and red triangles represent B_2 values estimated using Eq. (19) when all four, first three, or last three state points were used, respectively.

where $T_{0.9}$ is the temperature corresponding to reduced temperature of 0.9 and $T_{0.9}$ represents the isothermal temperature.

Subtracting Eq. (23) from Eq. (22) gives

$$B_2(T_{IT}) - B_2(T_{0.9}) = B \left(\frac{1}{T_{IT}} - \frac{1}{T_{0.9}} \right) + C \left(\frac{1}{T_{IT}^3} - \frac{1}{T_{0.9}^3} \right) \quad (24)$$

The intercept of $\frac{U - U^{ig}}{\rho RT}$ with respect to ρ gives the value of $\beta \frac{\partial B_2}{\partial \beta}$

$$\beta \frac{\partial B_2}{\partial \beta} = \frac{B}{T_{0.9}} + \frac{3C}{T_{0.9}^3} \quad (25)$$

Solving three equations (Eq. (22), (24), and (25)) with three unknowns gives the values of A, B, and C, hence a correlation for B_2 with respect to temperature is derived. Fig. 12 shows a correlation obtained by this method.

This method is successful for B_2 calculations, however B_3 calculation using Eq. (19) is less accurate, as shown in Fig. 13. Fortunately, according to Fig. 10 and Fig. 6, it is not important to obtain an accurate value of B_3 as long as the value of $(Z - 1)/\rho$ is accurately represented.

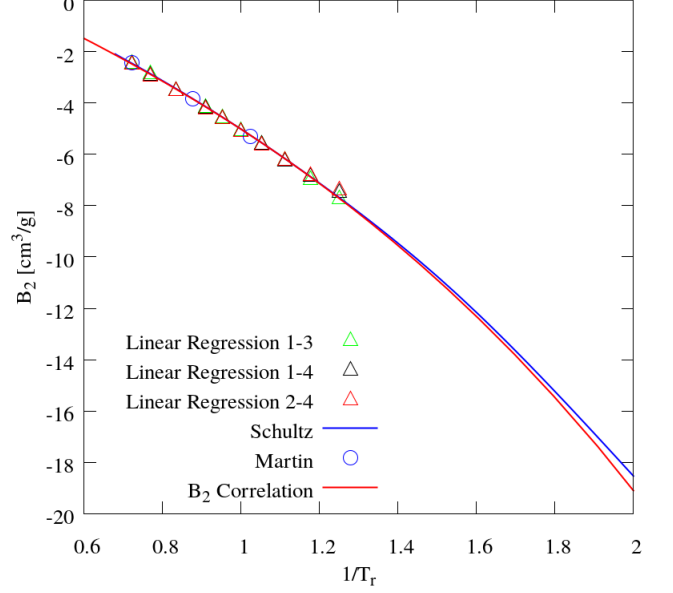


FIG. 12. Second virial coefficient calculated with various methods. Black, red, and green triangles are B_2 values calculated using 1-4, 2-4, and 1-3 linear regressions, respectively. 1-4, 1-3, or 2-4 mean all four, first three, or last three state points were used in calculating B_2 . The blue circles represent B_2 values obtained by Martin and Siepmann⁴ using a Monte Carlo method²⁰. B_2 correlation is in good agreement with Schultz's simulation results¹⁸.

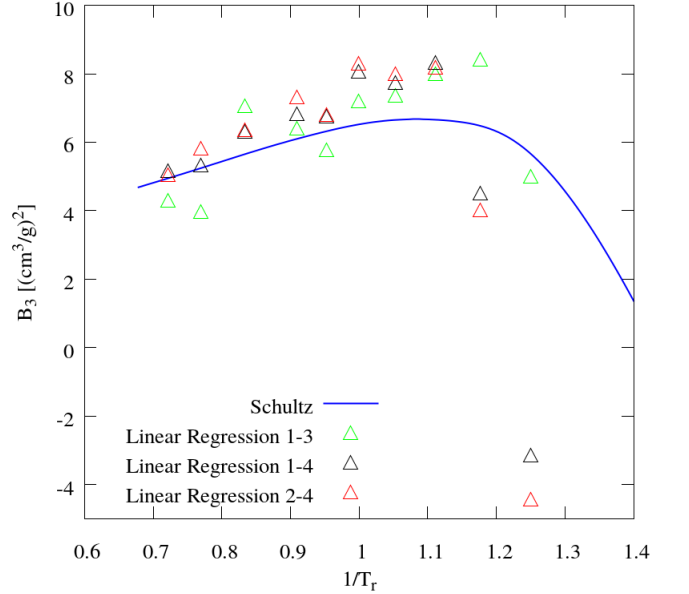


FIG. 13. Third virial coefficient calculated with various methods

V. FINITE SIZE EFFECTS

According to Fig. 6, P^{sat} accuracy is sensitive to accuracy of B_2 values at isothermal temperature (B_2^{IT}). This sensitivity is due to accumulation of errors when integrating along isotherm, such that an error in B_2^{IT} affects the A^{dep} values at all other points along the isotherm and isochores. Similarly, one would expect a significant influence from low density points, i.e. points 1, 2, and 3 in Fig. (1). Therefore, it is important to investigate the factors affecting the accuracy of Z at low densities on isotherm. The factors considered in this study are system size, the choice of MD or MC, and the choice of fixed bonds or flexible bonds.

The system size effects at low densities are demonstrated in Fig. 14-16. Plot of $(Z - 1)/\rho$ with respect to ρ shown in Fig. 14 demonstrates the effect of varying number of molecules in MD simulation of ethane in canonical ensemble. In order to match the $B_2 + B_3\rho + B_4\rho^2$ line which represents the exact values of $(Z - 1)/\rho$, we need 3200 ethane molecules to achieve low enough uncertainties for accurate extrapolation of B_2 for the simulation times chosen. In this plot C-C bonds are held constant using SHAKE algorithm²².

The effect of using flexible bonds is shown in Fig. 15. The systematic discrepancy from exact values (black line) as well as large uncertainties suggests that we should avoid flexible bonds at very low densities. A major problem with MD simulations with flexible bonds is the large pressure and energy fluctuations leading to the need for long equilibration and production times. Fig. 16 shows the low density NVT state points simulated using GOMC (GPU Optimized Monte Carlo) package¹⁹. This plot shows that MC method gives more reliable results than MD for low density NVT state points. Table III compares the uncertainties of Z when using different simulation methods. STD_1 represents the average of four relative standard deviations of Z (i.e., $\text{STD}/Z \times 100\%$), each calculated during a single run, while STD_2 is the relative standard deviation of Z from four separate runs. According to this table, the standard deviation from four replicate simulations (STD_2) are much smaller than the average standard deviation for a single run (STD_1). Therefore, Fig. 14-16 were plotted based on STD_2 uncertainties. Table III also shows that MC results have a much smaller STD_1 and STD_2 than rigid or flexible MD results.

Therefore, we recommend using MC when simulating these low density points. The choice of MD or MC for other high density state points in ITIC method shown in Fig. 1 is less important, because they generally agree with each other within their uncertainties. In this study, we used MC for all state points.

VI. SIMULATION DETAILS

In principle, both Monte Carlo and molecular dynamics methods can be used to simulate the NVT state

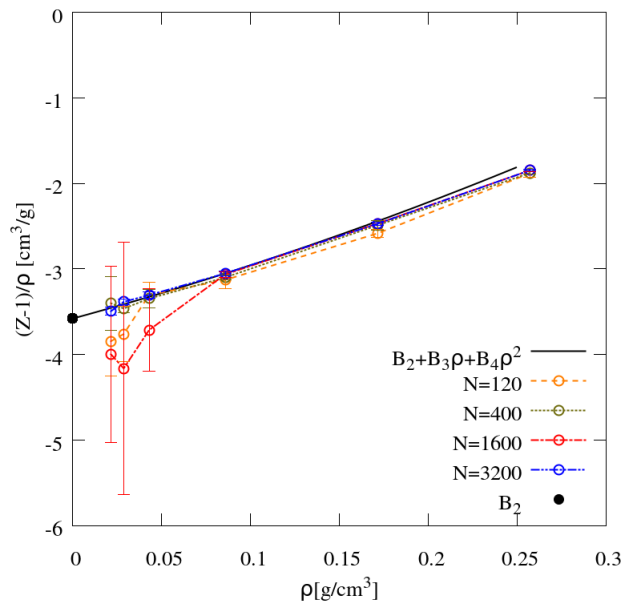


FIG. 14. Effect of number of ethane molecules on compressibility factor at low densities in MD simulation ($T^{\text{IT}} = 360$ K). State points are simulated in LAMMPS with SHAKE algorithm to keep the C-C bond constant. Solid black line represents $B_2 + B_3\rho + B_4\rho^2$ line where B_{2-4} are obtained from Schultz's work.¹⁸ Solid black circle shows the Schultz's value of B_2 . Note that the increasing deviation between black line and simulation points at higher densities is due to truncation of virial equation at B_4 . The error bars illustrate the standard deviation calculated based on four separate runs with different initial configurations.

points required to construct the isothermal and isochoric paths in the ITIC method. In this study, the MC method with fixed bond lengths was favored due to lower fluctuations. The Cassandra package²⁵ was used to simulate ethane and n -dodecane systems in the NVT ensemble using the TraPPE-UA potential model. In united-atom force fields, interaction sites may consist of a group of atoms, which is centered on the main atom of the group for the TraPPE-UA method²⁶. In TraPPE-UA model van der Waals interactions are truncated at 14 \AA and standard analytical long-range corrections are applied to compensate for truncation effects on energy and pressure²⁷. In TraPPE-UA, the bond lengths are considered fixed and the bond energy is zero. This approximation results in less pressure fluctuation at low densities, but we note that the MC results at high densities were consistent with MD results simulated in LAMMPS²⁸ within their uncertainties.

Packmol²⁹ package was used to create the initial configurations. The simulation boxes contained 1200 sites except for the four simulations required for estimating B_2 at isotherm temperature (the purple and green points in Fig. 1) for which simulation boxes contained 4800 sites. Standard Periodic Boundary Conditions (PBCs)

TABLE III. Compressibility factor and uncertainty at low densities. STD_1 represents the average of four relative standard deviations each calculated during the corresponding individual runs, while STD_2 is the relative standard deviation of Z from four separate runs.

Method	$\rho[\text{g}/\text{cm}^3]$	N=120		N=400		N=1600		N=3200	
		$STD_1\%$	$STD_2\%$	$STD_1\%$	$STD_2\%$	$STD_1\%$	$STD_2\%$	$STD_1\%$	$STD_2\%$
MC-rigid	0.0214	1.05	0.10	0.62	0.05	0.46	0.05	-	-
MC-rigid	0.0286	1.27	0.11	0.69	0.06	0.55	0.06	-	-
MC-rigid	0.0429	1.60	0.17	0.96	0.00	0.76	0.11	-	-
MC-rigid	0.0857	2.54	0.23	1.59	0.08	1.38	0.17	-	-
MC-rigid	0.1714	4.54	0.26	3.16	0.26	2.91	0.30	-	-
MC-rigid	0.2571	6.55	0.60	4.62	0.63	4.32	0.25	-	-
MD-rigid	0.0214	11.71	0.94	6.31	0.72	3.20	2.41	2.30	0.10
MD-rigid	0.0286	13.56	1.02	7.33	0.16	3.80	4.78	2.60	0.11
MD-rigid	0.0429	17.30	0.76	9.46	0.53	4.79	2.45	3.23	0.20
MD-rigid	0.0857	28.35	1.14	15.01	0.36	7.49	0.39	5.15	0.36
MD-rigid	0.1714	49.89	1.53	25.46	1.73	13.56	0.55	9.15	0.64
MD-rigid	0.2571	65.65	2.44	35.96	0.75	18.38	0.52	12.57	0.47
MD-flexible	0.0214	106.25	1.39	59.51	0.88	29.67	0.78	19.12	0.56
MD-flexible	0.0286	113.52	2.01	61.35	0.45	30.83	0.66	20.39	0.59
MD-flexible	0.0429	129.34	3.16	65.61	0.71	35.84	0.32	22.10	0.34
MD-flexible	0.0857	152.29	2.52	83.85	1.15	42.60	1.20	27.49	0.33
MD-flexible	0.1714	196.67	2.49	101.51	2.90	53.94	0.82	38.10	0.46
MD-flexible	0.2571	227.96	0.94	125.42	1.28	58.77	1.60	42.61	0.87

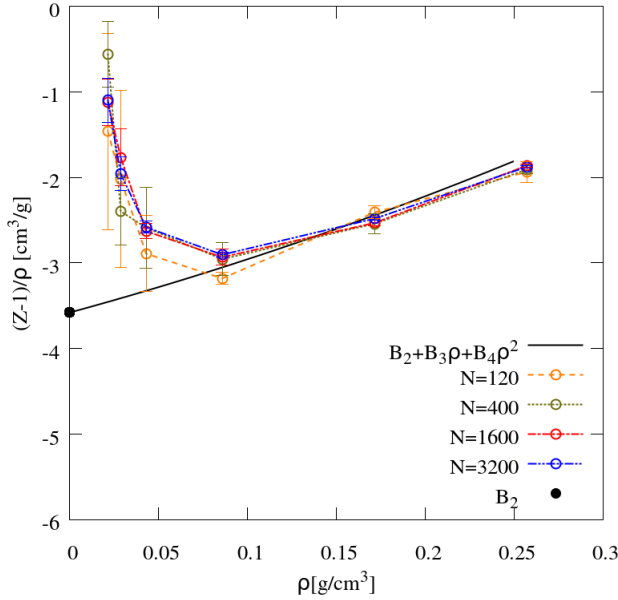


FIG. 15. Effect of number of ethane molecules on compressibility factor at low densities in MD simulation ($T^{\text{IT}} = 360 \text{ K}$). State points are simulated in LAMMPS with flexible C-C bonds. The bond constant was obtained from Nath et al.²³. The simulations were run using multiple-time-step algorithm RESPA²⁴.

was used. Simulations were run for 30 million Monte Carlo steps (MCS), and the last 15 million MCS were used for calculating the properties which were stored every 50,000 MC steps. For each compound, 22 NVT

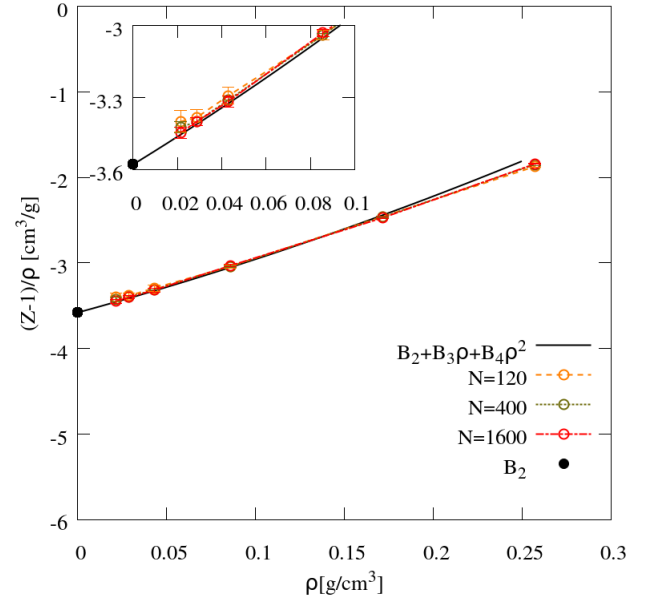


FIG. 16. Effect of number of ethane molecules on compressibility factor at low densities in MC simulation ($T^{\text{IT}} = 360 \text{ K}$). State points are simulated in GOMC.

points were simulated in order to obtain 5 saturation points as illustrated in Fig. 1. The density of the isochore with highest density was picked to match the experimental liquid density at the minimum reduced saturation temperature (T_r^{min}) of 0.45. Isothermal reduced temperatures for ethane and n -dodecane were 1.18 and 1.05, respectively. Density and temperature of simulated

state points for all simulated compounds are listed in supplementary material along with pressure and energies averages from Cassandra simulation at each point.

A. Internal Energy Departure Function Calculation

The internal energy departure function in Eq. (8) was calculated for isochoric points using Eq. (26)

$$U^{\text{dep}} = \frac{E^{\text{tot}} - E^{\text{bonded}} - E^{\text{intra}}}{NRT} \quad (26)$$

where E^{tot} , E^{bonded} , and E^{intra} are the total potential energy, bonded energy (bond, angle, and dihedral), and intramolecular pairwise energy (coulombic and van der Waals). N represents the number of molecules in the simulation box, R is the gas constant (8.3144598 J/(mol.K)), and T represents the temperature. Failing to subtract E^{intra} causes a significant error in vapor pressure. A post-processing code is required to calculate this quantity, if the molecular simulation package does not provide an internal way of estimating it (e.g. LAMMPS). In this case it is necessary to output the site coordinates a few times during the simulation.

B. Bootstrapping Method for Uncertainty Calculation

Bootstrapping was used to calculate the statistical uncertainties³⁰. Four series of independent NVT simulations were performed for each compound using different random number generator seeds. The NVT state points required for ITIC analysis were then randomly selected from the four series of NVT state points. This process was repeated 500 times and ITIC analysis was performed each time on the resulting set of randomly selected NVT points. The standard deviations were then calculated from the resulting 500 ITIC outputs. The bootstrap standard deviations are represented in Fig. 17-22 and provided in Tables IV-VI. Note that the ITIC method determines saturation conditions at a fixed value of ρ_{liq} (equal to the isochoric density) and, therefore, the bootstrap uncertainty in ρ_{liq} is zero.

C. Critical Pressure Calculation

The critical temperatures and densities can be estimated by the law of rectilinear diameter³¹ and the density scaling law³² for critical temperature

$$\frac{\rho_{\text{liq}} + \rho_{\text{vap}}}{2} = \rho_c + A(T_c - T) \quad (27)$$

$$\rho_{\text{liq}} - \rho_{\text{vap}} = B(T_c - T)^{0.325} \quad (28)$$

where A and B are constants that are fit to simulation data.

Critical pressure and acentric factor were calculated by plugging critical temperature obtained from Eq. (27) and Eq. (28) into Lee-Kesler equation³³ and fitting vapor pressure and saturation temperatures.

$$\ln \frac{P}{P_c} = f^{(0)} + \omega f^{(1)} \quad (29)$$

where P_c and ω represent critical pressure and acentric factor, respectively. $f^{(0)}$ and $f^{(1)}$ terms are defined in Eq. (30)

$$\begin{aligned} f^{(1)} &= 15.2518 - \frac{15.6875}{T_r} - 13.4721 \ln(T_r) + 0.43577 T_r^6 \\ f^{(0)} &= 5.92714 - \frac{6.09648}{T_r} - 1.28862 \ln(T_r) + 0.169347 T_r^6 \end{aligned} \quad (30)$$

D. Enthalpy of Vaporization Calculation

In ITIC method, enthalpy of vaporization (ΔH_v) is calculated using Eq. (31)

$$\Delta H_v = (H_{\text{vap}}^{\text{dep,sat}} - H_{\text{liq}}^{\text{dep,sat}})RT \quad (31)$$

where R is gas constant and H^{dep} is defined as

$$H^{\text{dep}} = \frac{H - H^{\text{ig}}}{RT} \quad (32)$$

$H_{\text{vap}}^{\text{dep,sat}}$ and $H_{\text{liq}}^{\text{dep,sat}}$ are unitless enthalpy departure functions of saturated vapor and liquid, respectively, which can be calculated by subtracting the ideal gas contribution from both sides of $H = U + PV$

$$H_{\text{liq}}^{\text{dep,sat}} \approx U_{\text{liq}}^{\text{dep,sat}} + Z_{\text{liq}} - 1 \quad (33)$$

$$H_{\text{vap}}^{\text{dep,sat}} \approx U_{\text{vap}}^{\text{dep,sat}} + Z_{\text{vap}} - 1 \quad (34)$$

The value of $U_{\text{liq}}^{\text{dep,sat}}$, as explained in Section II, is calculated at each fixed-point iteration based on the updated value of T^{sat} . According to Eq. 21, the value of $U_{\text{vap}}^{\text{dep,sat}}$ is approximated by taking the derivative of B_2 with respect to β as shown in Eq. (35).

$$U_{\text{vap}}^{\text{dep,sat}} \approx \rho_{\text{vap}} \beta \frac{dB_2}{d\beta} \approx \frac{\rho_{\text{vap}}}{T^{\text{sat}}} \frac{B_2^{\text{sat}} - B_2^{\text{IT}}}{\frac{1}{T^{\text{sat}}} - \frac{1}{T^{\text{IT}}}} \quad (35)$$

VII. EXAMPLE SIMULATIONS

The TraPPE-UA^{4,34,35}, Mie-UA^{5,36-38}, and TITP4P/2005³⁹ models were chosen for the purpose of testing the ITIC method due to the availability

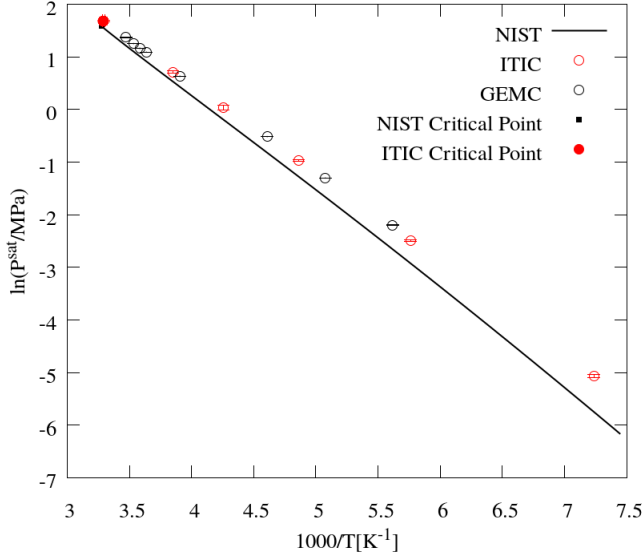


FIG. 17. P^{sat} plot of TraPPE-UA ethane. The virial expansion shown in Eq. (11) was truncated at the B_2 term. GEMC data were obtained from Ref. 4.

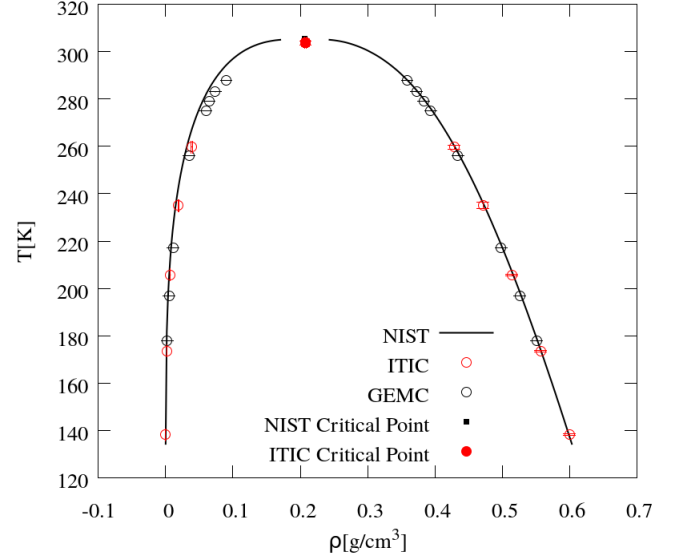


FIG. 18. Coexistence curves for TraPPE-UA ethane. The virial expansion shown in Eq. (11) was truncated at the B_2 term. GEMC data were obtained from Ref. 4.

of literature simulation results^{4,5,40,41}. As mentioned in Section VI, pure ethane and *n*-dodecane systems were simulated using Cassandra package²⁵ in the canonical ensemble to obtain the NVT state points. The saturation points calculated using the ITIC method were then compared against TraPPE-UA results obtained using Gibbs Ensemble Monte Carlo method (GEMC) which are available from the TraPPE website.⁴⁰ Fig. 17-18 show this comparison for ethane and Fig. 19-20 provide this information for *n*-dodecane. The isothermal/isochoric plots of A^{dep} , U^{dep} , Z , ΔH_v , and B_2 for all example simulations are included in supplementary material.

The ITIC method was also compared to histogram-reweighting Monte Carlo in the grand canonical ensemble (GCMC). *n*-Dodecane was simulated with Cassandra using Mie-UA potential parameters⁵. GCMC results in Fig. 21 and Fig. 22 are not available below a minimum reduced temperature (T_r^{min}) of 0.67, however the ITIC method allowed us to calculate vapor pressure and liquid densities for reduced temperatures as low as 0.45. In this simulation B_3 was not used and a B_2 correlation was obtained using the method described in Section IV. Fig. 23 shows the supercritical isotherm and the state points used for B_2 calculation.

In order to validate the ITIC method for polar molecules, the results of the ITIC method using TIP4P/2005 water simulated in Cassandra were compared against TIP4P/2005 data from NIST Standard Reference Simulation⁴¹ simulated using grand-canonical Wang-Landau/Transition-matrix Monte Carlo and histogram re-weighting. Fig. 24 and Fig. 25 shows the agreement between the two methods for TIP4P/2005 water. The absolute average deviation percent between vapor

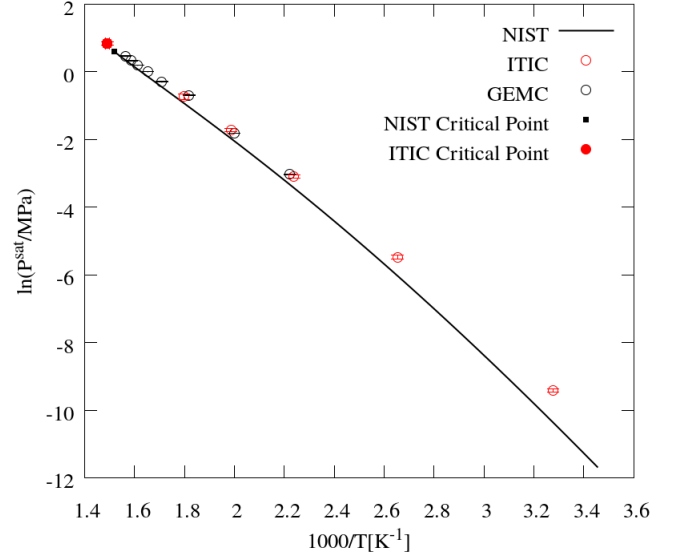


FIG. 19. P^{sat} plot of TraPPE-UA *n*-dodecane. The virial expansion shown in Eq. (11) was truncated at the B_2 term. GEMC data were obtained from Ref. 4.

pressure calculated using ITIC method and NIST simulation data for TIP4P/2005 water shown in Fig. 24 is less than 3 %.

TABLE IV. ITIC method saturation properties and uncertainties for ethane using TraPPE-UA model. Virial expansion was truncated at B_2 . ITIC uncertainties correspond to bootstrap standard deviations.

T_r^{sat}	T^{sat} [K]	\pm	P^{sat} [MPa]	\pm	ρ_{liq} [g/cm ³]	ρ_{vap} [g/cm ³]	\pm	ΔH_v [kJ/mol]	\pm
0.85	259.66	0.88	2.03290	0.04847	0.4286	0.038454	0.001116	9.587	0.041
0.77	235.00	1.33	1.03560	0.04182	0.4714	0.018879	0.000761	11.243	0.027
0.67	205.72	0.32	0.37902	0.00524	0.5143	0.007212	0.000096	12.626	0.003
0.57	173.57	0.30	0.08321	0.00147	0.5571	0.001780	0.000029	13.804	0.002
0.45	138.20	0.28	0.00632	0.00017	0.6000	0.000166	0.000004	14.868	0.003

TABLE V. ITIC method saturation properties and uncertainties for *n*-dodecane using TraPPE-UA model. Virial expansion was truncated at B_2 . ITIC uncertainties correspond to bootstrap standard deviations.

T_r^{sat}	T^{sat} [K]	\pm	P^{sat} [MPa]	\pm	ρ_{liq} [g/cm ³]	ρ_{vap} [g/cm ³]	\pm	ΔH_v [kJ/mol]	\pm
0.85	556.30	3.97	0.47993	0.037368	0.5336	0.021841	0.0019474	33.733	0.280
0.77	503.62	1.99	0.18021	0.009544	0.5870	0.008069	0.0004412	39.463	0.081
0.68	446.81	1.14	0.04585	0.002087	0.6404	0.002177	0.0000986	44.564	0.032
0.57	376.92	0.95	0.00419	0.000210	0.6937	0.000229	0.0000111	49.517	0.021
0.46	305.16	0.68	0.00008	0.000005	0.7471	0.000005	0.0000003	54.757	0.008

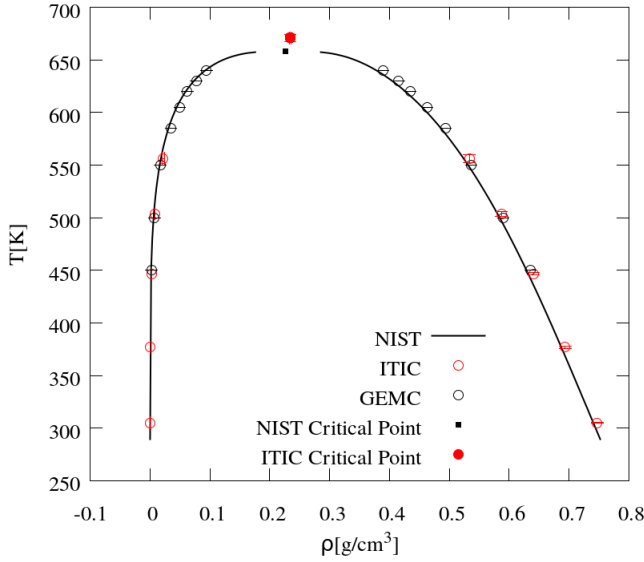


FIG. 20. Coexistence curves for TraPPE-UA *n*-dodecane. The virial expansion shown in Eq. (11) was truncated at the B_2 term. GEMC data were obtained from Ref. 4.

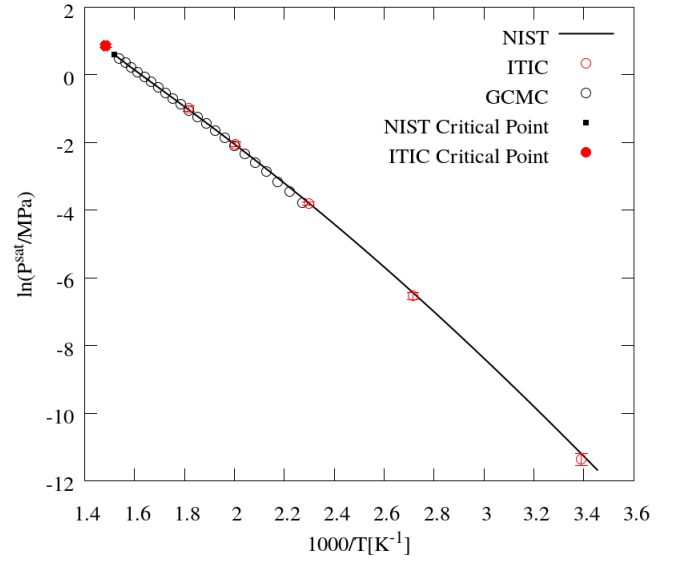


FIG. 21. Clausius-Clapeyron plot of Mie-UA *n*-dodecane. GCMC data were obtained from Potoff's work⁵.

VIII. CONCLUSIONS

Isothermal-isochoric integration method (ITIC) was shown to be a reliable alternative for phase equilibrium calculations. Validation against NIST REFPROP values showed that, in the absence of simulation uncertainty, the vapor pressure calculated by ITIC method with 9 points on IT and 3 points on IC sufficed to reproduce NIST REFPROP vapor pressure within 0.2 % deviation. ITIC is sensitive to low density NVT simulations and

the noise issue at low densities can be addressed by simulating larger systems, and preferring MC methods with fixed bond lengths when feasible.

It is important for engineering applications to be able to simulate systems at temperatures as low as $T_r = 0.45$ ⁴⁴. Monte Carlo methods such as GEMC and GCMC usually have a minimum reduced temperature limit of about 0.6⁴. The ITIC method, hence, outperforms GEMC and GCMC when T_r is less than 0.6. This method, on the other hand, is less favorable at high reduced temperatures, especially above $T_r = 0.85$, mostly

TABLE VI. ITIC method saturation properties and uncertainties for *n*-dodecane using Mie-UA model. Virial expansion was truncated at B_2 . ITIC uncertainties correspond to bootstrap standard deviations.

T_r^{sat}	T^{sat} [K]	\pm	P^{sat} [MPa]	\pm	ρ_{liq} [g/cm ³]	ρ_{vap} [g/cm ³]	\pm	ΔH_v [kJ/mol]	\pm
0.84	550.30	3.95	0.37071	0.030178	0.5336	0.016258	0.0014257	38.433	0.270
0.76	499.12	2.59	0.12778	0.008755	0.5870	0.005632	0.0003811	44.633	0.106
0.66	435.23	1.14	0.02235	0.001169	0.6404	0.001073	0.0000548	50.447	0.051
0.56	368.28	2.15	0.00146	0.000158	0.6937	0.000081	0.0000084	56.281	0.029
0.45	294.97	1.99	0.00001	0.000002	0.7471	0.000001	0.0000001	62.700	0.037

TABLE VII. ITIC method saturation properties for water using TIP4P/2005 model. Virial expansion was truncated at B_2 . ITIC uncertainties are not reported due to high computational cost of replicate simulations.

T_r^{sat}	T^{sat} [K]	P^{sat} [MPa]	ρ_{liq} [g/cm ³]	ρ_{vap} [g/cm ³]	ΔH_v [kJ/mol]
0.87	563.50	4.30448	0.7129	0.020456	33.56
0.81	526.26	2.32442	0.7841	0.011181	36.64
0.73	471.35	0.74423	0.8554	0.003659	40.57
0.63	405.95	0.11965	0.9267	0.000651	44.47
0.47	301.91	0.00093	0.9980	0.000007	49.98

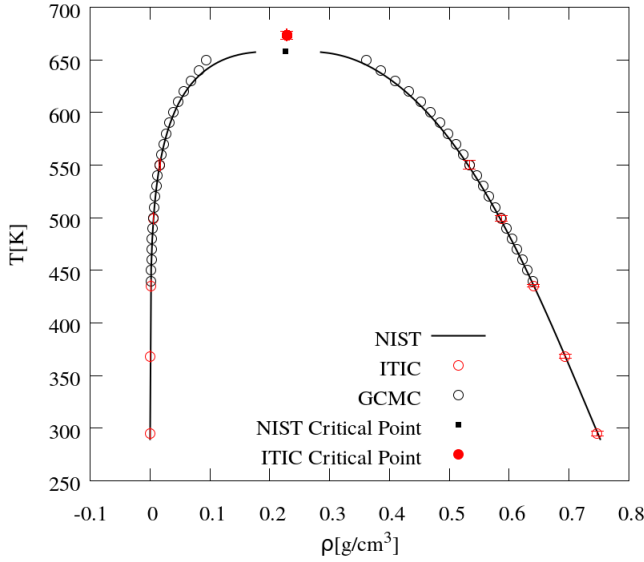


FIG. 22. Coexistence curves for Mie-UA *n*-dodecane. GCMC data were obtained from Potoff's work⁵.

due to lack of a convenient method to characterize the virial coefficients. MC methods can be used when the temperature is above $T_r = 0.6$, but if applications below 0.6 are of prospective interest, then MC methods lose their efficiency advantage, because in ITIC method, the entire isotherm must be generated.

In conclusion, it is recommended to approach the problem of coexistence calculation with a combination of Monte Carlo (GEMC or GCMC) and isothermal-isochoric integration in order to cover the entire range of industrially relevant temperatures. If a single method

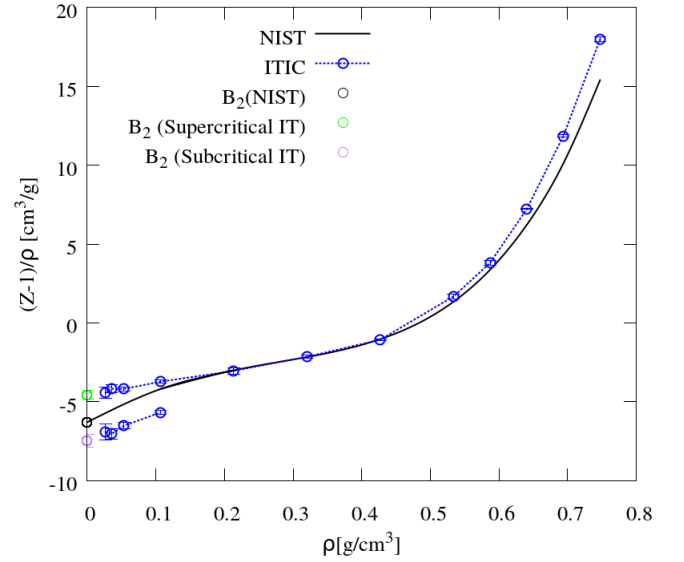


FIG. 23. Compressibility factor plot of Mie-UA *n*-dodecane. The lower isotherm was simulated to calculate the purple point, i.e. the B_2 value at $T_r = 0.9$.

is preferred, or if MD is the preferred simulation method, ITIC can easily be implemented from $T_r = 0.85$ to 0.45 with less than 50 % additional computational time requirement over the combined method.

IX. ACKNOWLEDGMENTS

This research was performed while R.A.M. held a National Research Council (NRC) Postdoctoral Research

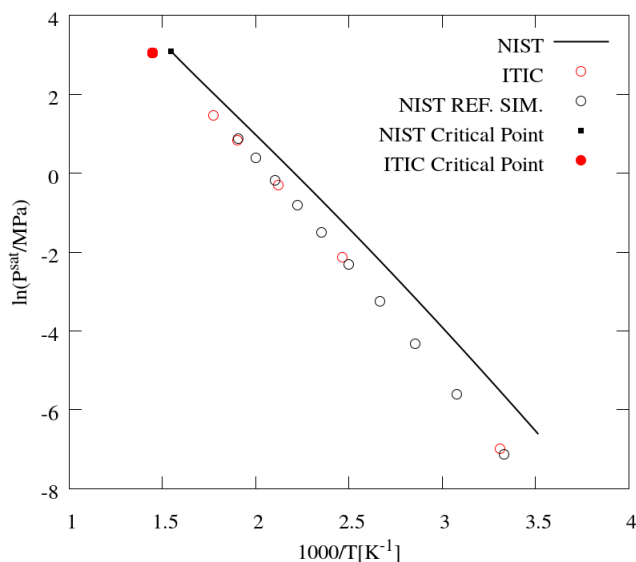


FIG. 24. Clausius-Clapeyron plot of TIP4P/2005 water. GCMC data were obtained from NIST Standard Reference Simulation website⁴¹. B_2 values at saturation temperatures were obtained from Benjamin et al.⁴² and Chiavo et al.⁴³.

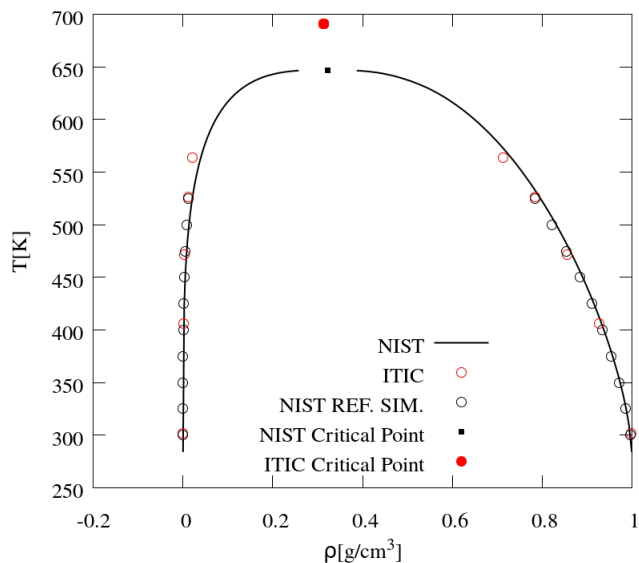


FIG. 25. Coexistence curves for TIP4P/2005 water. GCMC data were obtained from NIST Standard Reference Simulation website⁴¹.

Associateship at the National Institute of Standards and Technology (NIST). Contribution of NIST, an agency of the United States government; not subject to copyright in the United States.

X. SUPPLEMENTARY MATERIAL

See supplementary material for density, temperature, Z and energies of simulated state points for all simulated compounds, as well as the isothermal/isochoric plots of A^{dep} , U^{dep} , Z , ΔH_v , and B_2 for all example simulations.

XI. REFERENCES

- ¹D. Frenkel and B. Smit, *Understanding Molecular Simulation: from Algorithms to Applications* (Academic Press, San Diego, 1996).
- ²A. Z. Panagiotopoulos, *Molecular Physics* **61**, 813 (1987).
- ³A. S. Paluch, V. K. Shen, and J. R. Errington, *Industrial & Engineering Chemistry Research* **47**, 4533 (2008).
- ⁴M. G. Martin and J. I. Siepmann, *The Journal of Physical Chemistry B* **102**, 2569 (1998).
- ⁵J. J. Potoff and D. A. Bernard-Brunel, *The Journal of Physical Chemistry B* **113**, 14725 (2009).
- ⁶D. Y. Peng and D. B. Robinson, *Industrial and Engineering Chemistry Fundamentals* **15**, 59 (1976).
- ⁷D. A. Kofke, *The Journal of Chemical Physics* **98**, 4149 (1993).
- ⁸M. G. Ahunbay, S. Kranias, V. Lachet, and P. Ungerer, *Fluid Phase Equilibria* **224**, 73 (2004).
- ⁹J. R. Elliott and L. Hu, *The Journal of Chemical Physics* **110**, 3043 (1999).
- ¹⁰N. F. Carnahan, *The Journal of Chemical Physics* **51**, 635 (1969).
- ¹¹C. Nieto-Draghi, G. Fayet, B. Creton, X. Rozanska, P. Rotureau, J. C. De Hemptinne, P. Ungerer, B. Rousseau, and C. Adamo, *Chemical Reviews* **115**, 13093 (2015).
- ¹²R. L. Burden and J. Douglas Faires, *Numerical analysis* (Prindle, Weber & Schmidt, 1985).
- ¹³E. W. Lemmon, M. L. Huber, and M. O. McLinden, "NIST Standard Reference Database 23: Reference Fluid Thermodynamic and Transport Properties-REFPROP, Version 9.1, National Institute of Standards and Technology," (2013).
- ¹⁴D. Bücker and W. Wagner, *Journal of Physical and Chemical Reference Data* **35**, 205 (2006), <https://doi.org/10.1063/1.1859286>.
- ¹⁵K. E. Atkinson, *An introduction to numerical analysis* (John Wiley & Sons, 2008).
- ¹⁶E. W. Lemmon and M. L. Huber, *Energy & Fuels* **18**, 960 (2004), <https://doi.org/10.1021/ef0341062>.
- ¹⁷W. Wagner and A. Pruß, *Journal of Physical and Chemical Reference Data* **31**, 387 (2002), <https://doi.org/10.1063/1.1461829>.
- ¹⁸A. J. Schultz and D. A. Kofke, *The Journal of Chemical Physics* **133** (2010), 10.1063/1.3486085.
- ¹⁹J. Mick, E. Hailat, V. Russo, K. Rushaidat, L. Schwiebert, and J. Potoff, *Computer Physics Communications* **184**, 2662 (2013).
- ²⁰V. I. Harismiadis and I. Szleifer, *Molecular Physics* **81**, 851 (1994).
- ²¹DIPPR, "Design Institute for Physical Property Data," (2004).
- ²²J. P. Ryckaert, G. Ciccotti, and H. J. C. Berendsen, *J. Comp. Phys.* **23**, 327 (1977).
- ²³S. K. Nath, F. A. Escobedo, J. J. de Pablo, and I. Patramai, *Industrial & Engineering Chemistry Research* **37**, 3195 (1998).
- ²⁴M. Tuckerman, B. J. Berne, and G. J. Martyna, *The Journal of chemical physics* **97**, 1990 (1992).
- ²⁵J. K. Shah, E. Marin-Rimoldi, R. G. Mullen, B. P. Keene, S. Khan, A. S. Paluch, N. Rai, L. L. Romanielo, T. W. Rosch, B. Yoo, and E. J. Maginn, *Journal of Computational Chemistry* **38**, 1727 (2017).
- ²⁶B. Smit, S. Karaborni, J. I. Siepmann, B. Smit, S. Karaborni, and J. I. Siepmann, **2126** (1998).
- ²⁷M. P. Allen and D. J. Tildesley, *Computer simulation of liquids* (Oxford university press, 2017).

- ²⁸S. Plimpton, P. Crozier, and A. Thompson, Sandia National Laboratories **18** (2007).
- ²⁹L. Martínez, R. Andrade, E. G. Birgin, and J. M. Martínez, Journal of computational chemistry **30**, 2157 (2009).
- ³⁰B. Efron, Biometrika **68**, 589 (1981).
- ³¹J. S. Rowlinson, “Liquids and Liquid Mixtures,” (1982).
- ³²J. S. Rowlinson and B. Widom, *Molecular theory of capillarity* (Courier Corporation, 2013).
- ³³B. I. Lee and M. G. Kesler, AIChE Journal **21**, 510 (1975).
- ³⁴M. G. Martin and J. I. Siepmann, The Journal of Physical Chemistry B **103**, 4508 (1999).
- ³⁵C. D. Wick, M. G. Martin, and J. I. Siepmann, The Journal of Physical Chemistry B **104**, 8008 (2000).
- ³⁶J. Mick, M. S. Barhaghi, and B. Jackman, [Journal of Chemical & \(2017\)](#).
- ³⁷M. S. Barhaghi, J. R. Mick, and J. J. Potoff, [Molecular Physics 115, 1378 \(2017\)](#).
- ³⁸J. R. Mick, M. Soroush Barhaghi, B. Jackman, K. Rushaidat, L. Schwiebert, and J. J. Potoff, The Journal of chemical physics **143**, 114504 (2015).
- ³⁹J. L. Abascal and C. Vega, [The Journal of chemical physics 123, 234505 \(2005\)](#).
- ⁴⁰B. L. Eggimann, A. J. Sunnarborg, H. D. Stern, A. P. Bliss, and J. I. Siepmann, Molecular Simulation **40**, 101 (2014).
- ⁴¹V. Shen, D. Siderius, W. Krekelberg, and H. E. Hatch, “[NIST Standard Reference Simulation Website](#),” (2008).
- ⁴²K. M. Benjamin, J. K. Singh, A. J. Schultz, and D. A. Kofke, [Journal of Physical Chemistry B 111, 11463 \(2007\)](#).
- ⁴³A. A. Chialvo, A. Bartók, and A. Baranyai, [Journal of Molecular Liquids 129, 120 \(2006\)](#).
- ⁴⁴R. C. Reid, J. M. Prausnitz, and B. Poling, *The Properties of Gases and Liquids*, 4th ed. (McGraw-Hill, New York, 1987).